Control of Giant Topological Magnetic Moment and Valley Splitting in Trilayer Graphene

Zhehao Ge,[1,*] Sergey Slizovskiy,[2,3,*] Frédéric Joucken,[1] Eberth A. Quezada,[1] Takashi Taniguchi,[4] Kenji Watanabe,[5] Vladimir I. Fal'ko,[2,3,6,†] and Jairo Velasco, Jr.[1,‡]

[1]*Department of Physics, University of California, Santa Cruz, California 95064, USA*
[2]*Department of Physics and Astronomy, University of Manchester, Oxford Road, Manchester M13 9PL, United Kingdom*
[3]*National Graphene Institute, University of Manchester, Booth Street East, Manchester M13 9PL, United Kingdom*
[4]*International Center for Materials Nanoarchitectronics National Institute for Materials Science, 1-1 Namiki, Tsukuba 305-0044, Japan*
[5]*Research Center for Functional Materials National Institute for Materials Science, 1-1 Namiki, Tsukuba 305-0044, Japan*
[6]*Henry Royce Institute for Advanced Materials, Manchester M13 9PL, United Kingdom*

(Received 28 March 2021; accepted 17 August 2021; published 23 September 2021)

Bloch states of electrons in honeycomb two-dimensional crystals with multivalley band structure and broken inversion symmetry have orbital magnetic moments of a topological nature. In crystals with two degenerate valleys, a perpendicular magnetic field lifts the valley degeneracy via a Zeeman effect due to these magnetic moments, leading to magnetoelectric effects which can be leveraged for creating valleytronic devices. In this work, we demonstrate that trilayer graphene with Bernal stacking (ABA TLG), hosts topological magnetic moments with a large and widely tunable valley g factor (g_ν), reaching a value $g_\nu \sim 1050$ at the extreme of the studied parametric range. The reported experiment consists in sublattice-resolved scanning tunneling spectroscopy under perpendicular electric and magnetic fields that control the TLG bands. The tunneling spectra agree very well with the results of theoretical modeling that includes the full details of the TLG tight-binding model and accounts for a quantum-dot-like potential profile formed electrostatically under the scanning tunneling microscope tip.

DOI: 10.1103/PhysRevLett.127.136402

The orbital magnetic moment stemming from the rotational motion of electrons is ubiquitous in nature. It can be found in a variety of systems from single atoms to complex crystals, and can influence the magnetic properties of these systems. In recent years, topological magnetic moments emerging from self-rotating wave packets [1] have been discovered in 2D van der Waals crystals with broken inversion symmetry [2–6]. Experimental manifestations of the topological magnetic moments have been observed lately, including the valley Zeeman effect [2–17], spontaneous orbital ferromagnetism [18,19], and orbital magnetoelectric effects [20–22]. The former is important for valleytronics because it enables control of individual valley states, while the latter two could potentially facilitate new ultralow power magnetic devices. To harness the valley Zeeman and orbital magnetoelectric effects in 2D crystals, systems with topological magnetic moments both large and tunable via gate modulation are desirable. The possibility to achieve these properties has been separately demonstrated with Bernal stacked bilayer graphene (BLG), offering [16] a tunable valley g factor $(g_v) \sim 40 - 120$, and moiré superlattices in graphene [4], with large $g_\nu \sim 2500$.

Here we realize a giant gate-tunable topological magnetic moment in naturally occurring Bernal stacked trilayer graphene (ABA TLG) by utilizing its peculiar band structure. Because of the mirror symmetry of ABA TLG [Fig. 1(a)], its electronic spectra can be viewed as overlapping BLG and weakly gapped monolayer (MLG) bands [23]. A full tight-binding calculation of the ABA TLG band structure in the absence of a perpendicular electric field is plotted in Fig. 1(b), where the effective MLG and BLG bands (both gapped) are indicated by the blue cones and semitransparent red shells, respectively. The gaps and mutual alignment of the two bands are tunable by the encapsulation environment, gating, and doping. This feature offers an opportunity to engage states with a large topological magnetic moment and therefore giant g_ν specific to weakly gapped monolayers [1,4,6]. This is because with a similar gap size, gapped MLG has a much larger orbital magnetic moment compared to gapped BLG (see further discussion in Supplemental Material [24] Sec. S12).

In this work we use scanning tunneling microscopy-spectroscopy (STM/STS) to measure this giant g_ν and study the tunable topological magnetic moments of the effective MLG band in ABA TLG. The ABA TLG and hexagonal boron nitride (hBN) heterostructure for our STS study is fabricated with a conventional polymer-based transfer method [25] (see Sec. S1 in Supplemental Material for sample fabrication details [24], which includes Refs. [26–29]). ABA TLG and hBN are misaligned intentionally to avoid any spectral reconstruction near the charge neutrality point (CNP) [30], which is the energetic region of interest in our study. The measurement setup for our experiments is

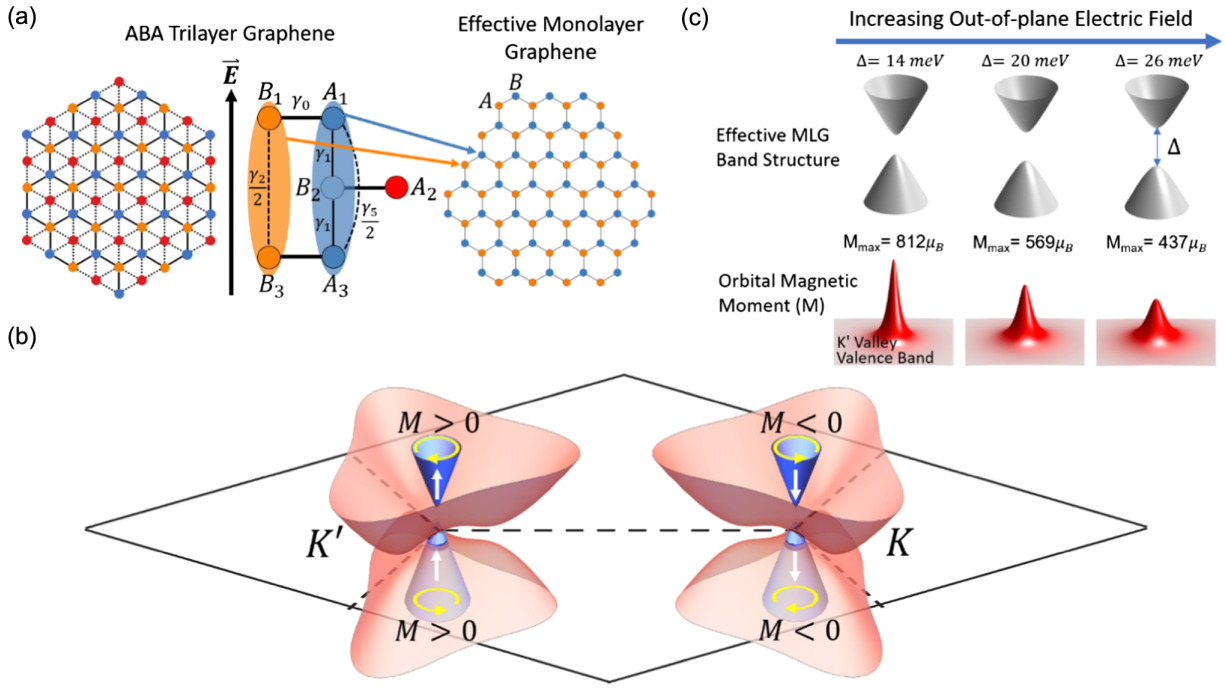

FIG. 1. Effective monolayer graphene (MLG) band in Bernal stacked trilayer graphene (ABA TLG) with giant and tunable topological magnetic moment. (a) Left panel: Top view of the ABA TLG atomic structure. Middle panel: Schematic of the ABA TLG unit cell and hopping parameters. Right panel: Mapping ABA TLG onto an effective MLG lattice. (b) Schematic of the calculated low energy band structure of ABA TLG with no external electric field in the K and K' valleys. Blue cones represent the effective MLG bands. The semitransparent red shells represent the effective BLG bands. The yellow arrows depict the orientation of the self-rotating wave packet in each band and the white arrows correspond to the direction of the topological magnetic moment originating from the self-rotating wave packet. (c) Upper panel: Low energy band structures of the effective gapped MLG with different out-of-plane electric fields applied to the ABA TLG. Lower panel: topological magnetic moment in the K' valley valence band of the corresponding gapped MLG bands shown in the upper panel. Here we assumed v_F of the MLG band is 10^6 m/s.

shown in the upper panel of Fig. 2(a). The STM tip is grounded, and a bias voltage V_S is applied between the STM tip and ABA TLG to induce a tunneling current. In addition, a backgate voltage V_G is applied between the doped silicon and ABA TLG to institute an out-of-plane electric field that shifts the TLG Fermi energy and modifies the TLG band structure [31]. To avoid influence from adsorbates we performed all STS measurements at the centers of atomically pristine regions that were no smaller than 20×20 nm^2 (see typical topography of such a region in SM Sec. S1 [24]). The lower panel of Fig. 2(a) shows a typical topography at the center of such a region where the tunneling spectra were acquired. A clear triangular lattice is visible, which agrees with prior STM studies of ABA TLG supported on metals and SiC [32,33]. Furthermore, no moiré pattern is observed in our topography scans, thus indicating the ABA TLG and hBN are indeed misaligned.

A model atomic structure is overlaid on top of the measured topography in Fig. 2(a) that indicates the ABA TLG sublattices (for sublattice identification method see in Supplemental Material Sec. S3 [24], which includes Ref. [34]). The gray and bright spots correspond to sublattices A_1 and B_1, respectively. Both of these sublattices reside on the top layer, as shown in Fig. 1(a). In contrast, the dark spot corresponds to sublattice A_2, which resides on the middle layer. Since STM is mostly sensitive to surface states, we expect the tunneling signal from our measurements to consist primarily of contributions from the top ABA TLG layer, hence sublattices A_1 and B_1 will dominate our STS measurements.

Typical gate resolved STS results for sublattices A_1 and B_1 are shown in Figs. 2(b) and 2(c), respectively. To reduce the influence of slight deviations from the target sublattice for a single measurement, the tunneling spectra at each gate voltage shown in Figs. 2(b) and 2(c) correspond to an average of spectra at nine different targeted locations (see Supplemental Material Sec. S4 for the STS results before averaging [24]). Interestingly, the spectra for sublattice A_1 exhibit a prominent dI/dV_S peak (marked by a black dot) that diminishes in intensity and shifts toward positive bias voltage with decreasing V_G. We find the strong dI/dV_S peak is only present on sublattice A_1 [Figs. 2(b) and 2(c)]. Notably, this feature was absent in previous gate resolved STS studies of ABA TLG [35,36].

Intrigued by this finding we next performed gate and sublattice resolved STS on the ABA TLG/hBN heterostructure in finite and out of plane magnetic field B. Our aim was to investigate the possibility of valley splitting in this system.

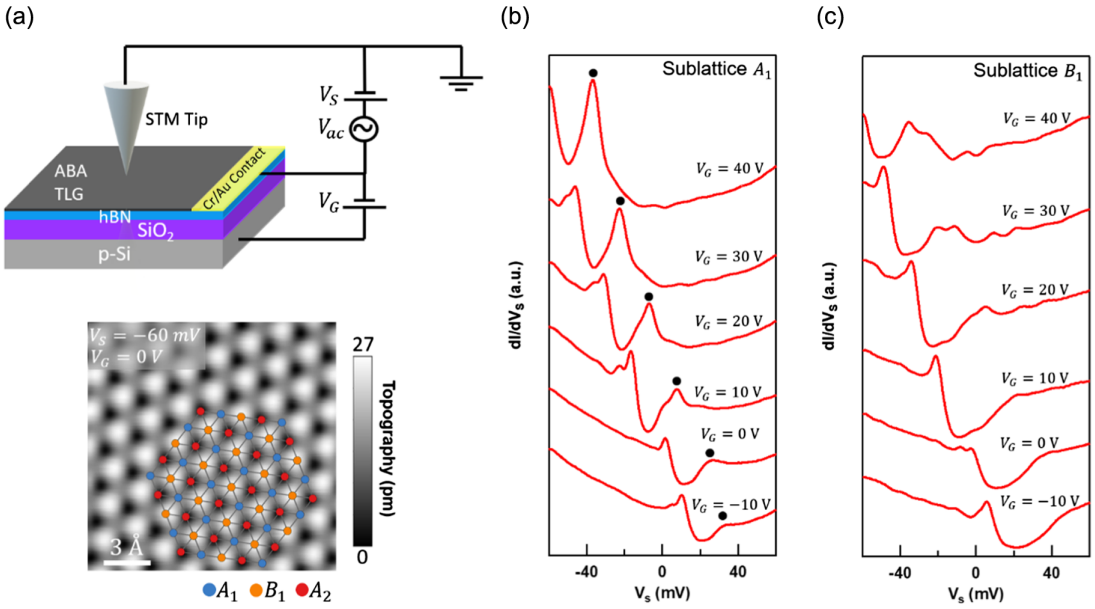

FIG. 2. Atomically resolved scanning tunneling spectroscopy (STS) of ABA TLG. (a) Upper panel: Schematic of the experimental setup. Lower panel: Atomically resolved topography of a pristine ABA TLG patch at $V_G = 0$ V, the scanning parameters used are $I = 1$ nA, $V_S = -60$ mV. The ABA TLG atomic structure is overlaid on top of the topography, the definition of the sublattice is consistent with that in Figs. 1(a) and 1(b). (b)–(c) Tunneling spectra at various gate voltages on sublattice A_1 (b) and B_1 (c). The set point used to acquire the tunneling spectra was $I = 1$ nA, $V_S = -60$ mV, with a 2 mV ac modulation.

Figure 3(a) shows the experimentally measured tunneling spectra on sublattice A_1 at $V_G = 30$ V with different B. The most prominent feature in these data is the strong dI/dV_S peak that splits into two as B is increased. This behavior was also observed at different V_G on sublattice A_1 but not on sublattice B_1 (see Supplemental Material Sec. S5 for additional data [24]). In addition, we found lower intensity satellite dI/dV_S peaks emerge on the positive V_S side as B is increased. In contrast to the prominent sublattice dependent peaks, these satellite dI/dV_S peaks were observed on both sublattices and at different V_G. Figure 3(b) shows the dependence of the peak splitting energy ΔE on B at $V_G = 30$ V as red dots, we find the relationship between ΔE and B is not linear. This nonlinear behavior is also observed at different V_G (see Supplemental Material Sec. S11 for additional data [24]).

The emergent dI/dV_S peak observed on sublattice A_1 and its splitting in B can be understood as resulting from a gapped MLG quantum dot (QD) with large topological magnetic moments. As shown in Fig. 1(a), the antisymmetric wave function combination of sublattices A_1 and A_3 (blue shading) and B_1 and B_3 (orange shading) can be mapped onto a new sublattice B and A of an effective MLG lattice that gives rise to effective MLG bands [31]. Because of the γ_2 and γ_5 hopping energy difference and the onsite energy difference between the trimer and non-trimer sites (Δ_{AB}), the effective MLG sublattices have different energies (broken inversion symmetry), leading to a light-mass Dirac spectrum with large topological magnetic moments.

Importantly, due to the capacitive coupling between the STM tip and ABA TLG, a shallow and smooth positive potential well is induced in ABA TLG, yielding an electrostatically defined QD [37,38]. As depicted in the lower left panel of Fig. 3(c), the positive potential well induced by the STM tip raises the energy of valence band MLG states into the bandgap, making these states localized and forming a valley degenerate QD state. This emerging QD state can explain the strong dI/dV_S peak on sublattice A_1 [Fig. 2(b)] where the MLG states near the valence band edge reside. A comparison between the calculated LDOS for ABA TLG with and without a tip potential well can be found in Supplemental Material Sec. S8 [24]. Importantly, the localized state assists experimental detection of valley splitting in low B (see discussion in Supplemental Material Sec. S9 [24]). Furthermore, with increasing V_G, the gap size (Δ) of the effective MLG band increases (see Supplemental Material Sec. S6 for Δ determination details [24], which includes Ref. [39]). This leads to an enhanced quantum confinement at higher V_G, which explains the increasing dI/dV_S peak height at higher V_G in Fig. 2(b).

By applying an out of plane B, the valley degeneracy of the effective MLG QD state is lifted, thus explaining the splitting of the observed peak in B. As schematized in Fig. 1(c), the topological magnetic moments $M_z(\vec{k}) = \tau(e/\hbar)\{\Delta/([\Delta/(\hbar v_F)]^2 + 4|\vec{k}|^2)\}$ (v_F is the Fermi velocity of the MLG bands, $\tau = +1$ and -1 for K' and K valley, respectively) of the effective MLG bands in K and K' valleys are both out of plane and with opposite orientations. Thus, an out of plane B will couple to the opposite $\vec{M} = \hat{z}\tau M_z$ of the electrons in the two valleys and generate valley splitting, as schematized in the lower right panel of Fig. 3(c). Using this simple picture, ΔE can be

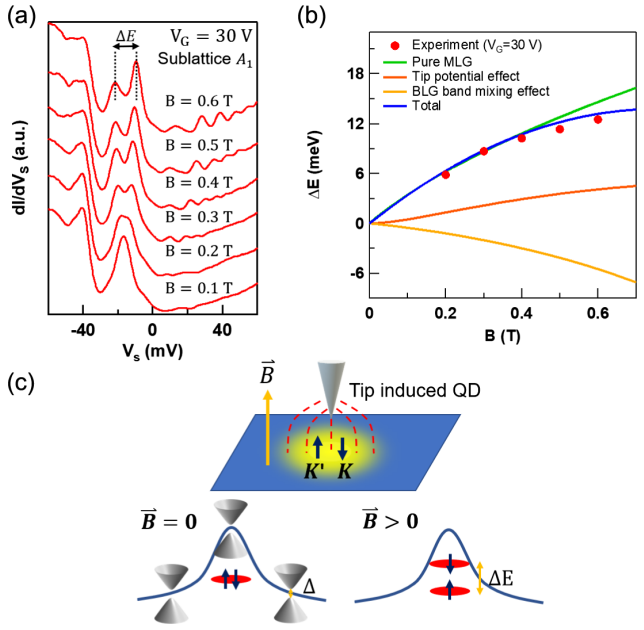

FIG. 3. Magnetic field controlled valley splitting in ABA TLG. (a) Tunneling spectra on sublattice A_1 at $V_G = 30$ V with different out of plane magnetic fields (B). The set point used to acquire the tunneling spectra was $I = 1$ nA, $V_S = -60$ mV, with a 2 mV ac modulation. (b) Comparison between the experimental and theoretical valley splitting energy at $V_G = 30$ V. The experimental splitting energy is extracted from (a). The depth and width of the Gaussian potential well used in the theoretical calculation are 50 meV and 40 nm, respectively. (c) Upper panel: Schematic of an STM tip induced quantum dot (QD) in ABA TLG. The black arrows represent the directions of topological magnetic moments in TLG K and K' valleys, which can couple to an external out of plane B (orange arrow). Lower left panel: Schematic of the tip induced QD potential profile. The blue line represents the charge neutrality point of gapped MLG, the red oval schematizes the QD state arising from confinement. The black arrows represent the degenerate valley degree of freedom. Lower right panel: Schematic of the QD state valley splitting under a B.

approximated as $2|\vec{M} \cdot \vec{B}|$, which can also be expressed as $g_\nu \mu_B B$. Here μ_B is the Bohr magneton, and g_ν is defined as the valley g factor. With increasing B, the magnetic field confinement starts to dominate over the QD localization, and the valley splitting is expected to gradually start following the splitting between the Landau level (LL) 0− and LL1−, which is nonlinear as plotted by the green line in Fig. 3(b). To fully account for the observed nonlinearity, we further consider the influence of the tip potential on LL0− and LL1− [red line in Fig. 3(b)] as well as the effect from the MLG/BLG band mixing induced by a vertical electric field [orange line in Fig. 3(b)]. After incorporating these additional effects in our theory, the predicted ΔE [blue line in Fig. 3(b)] shows good agreement with the experimentally extracted ΔE value in Fig. 3(b) (a more detailed discussion can be found in Supplemental Material Sec. S11 [24]).

Having understood the observed valley splitting in B for ABA TLG, we now discuss its gate tunability. The gap of the effective MLG band depends on the out-of-plane electric field (E_z), which can be expressed as $\Delta = \frac{1}{2}\sqrt{\gamma_2^2 + (U_1 - U_3)^2} + (\gamma_5/2) - \Delta_{AB}$. Here $U_1 - U_3 \propto E_z$ is the interlayer energy difference between the top and bottom layer of ABA TLG. Modulation of this quantity by V_G controls the intensity of the inversion symmetry breaking in the top TLG layer, which leads to a gate tunable MLG gap (Δ). Importantly, this tunable Δ will give rise to tunable topological magnetic moments in MLG bands. As shown in Fig. 1(c), by increasing Δ from 14 to 26 meV, the maximum value of the topological magnetic moment changes from 808 μ_B to 442 μ_B. Such gate tunable topological magnetic moments also yield a gate tunable g_ν.

To study the gate tunable g_ν in ABA TLG, we performed $dI/dV_S(V_S, B)$ measurements with different V_G. We first compare the experimental result with a simulation based on a full ABA TLG tight binding (TB) model with a potential well (details can be found in Supplemental Material Sec. S7 [24], which includes Refs. [40–48]. Figure 4(a) shows the second order derivative of a measured $dI/dV_S(V_S, B)$ with high B resolution, for which $V_G = 30$ V, the red features correspond to dI/dV_S peaks. The STM tip used to acquire these data lack clear atomic resolution, as a result, we expect the tunneling spectra in this dataset is a mixture of the states from sublattices A_1 and B_1. Additional sublattice resolved $dI/dV_S(V_S, B)$ color plots measured at a single V_G from a different STM tip can be found in Supplemental Material Sec. S14. Figure 4(b) is a simulated $\partial^2 \mathrm{LDOS}/\partial E^2(E, B)$ at $V_G = 30$ V, the LDOS from sublattice A_1 and B_1 are mixed together with a ratio of 10∶1 to better reflect the nature of the STM tip used for the associated measurements. The experiment and simulation display good qualitative agreement, at high B they both show a splitting peak and LLs below and above the Fermi level. Quantitative differences between the experiment and simulation can be attributed to parameter differences between the two such as the tip potential, local electric field, and hopping parameters, which are difficult to extract from the experiment.

We next obtain g_ν and demonstrate its gate tunability by performing linear fits to the split peaks in small B for different V_G. The linear splitting is expected from the simple picture of coupling between $\vec{M}$ and $\vec{B}$. Figure 4(c) shows the enlargement of $dI^3/dV_S^3(V_S, B)$ around the valley split peaks at $V_G = 10$ and 40 V, the nonlinear valley splitting is clearly visible. The yellow dashed lines are linear fits to the split peaks in small B (additional data analysis details and data can be found in Supplemental Material Sec. S13 [24]). Based on the slopes of these fitted lines we extracted a $g_\nu = 1050 \pm 72$ at $V_G = 10$ V and a $g_\nu = 517 \pm 47$ at $V_G = 40$ V. This result demonstrates g_ν in ABA TLG is both giant and gate tunable, the combination of which is unparalleled in previously studied systems [4,16].

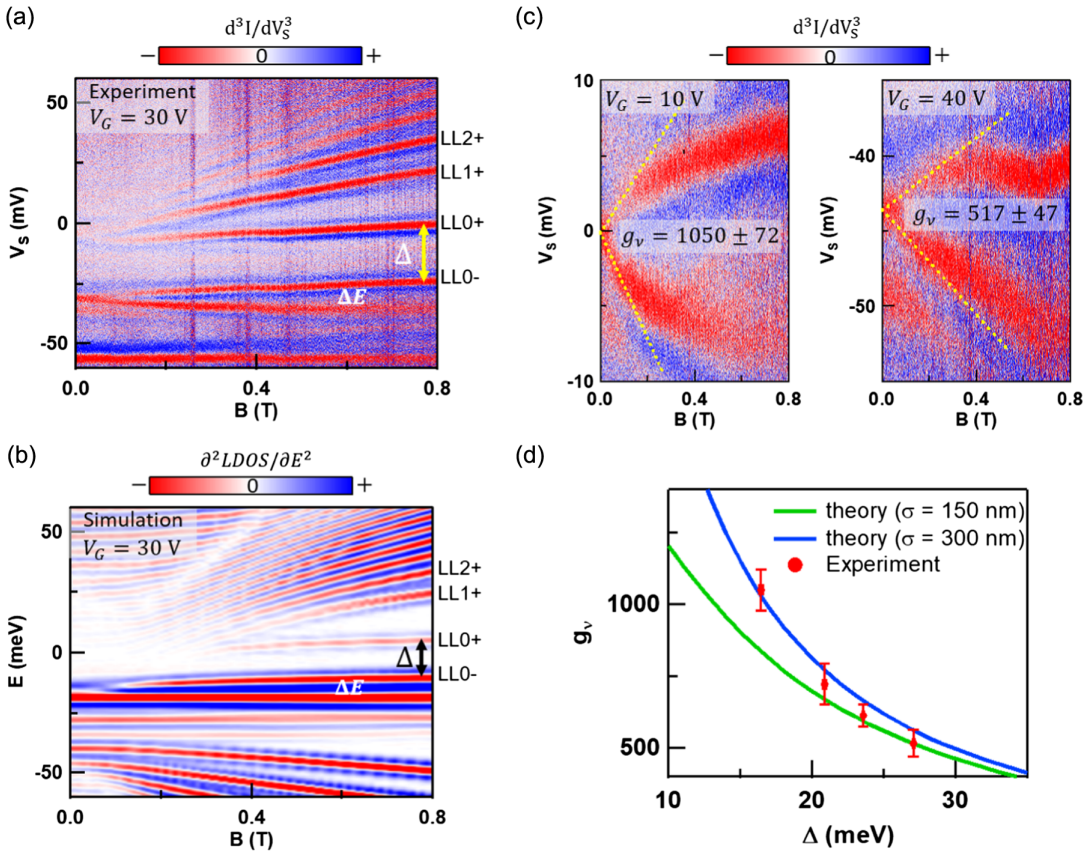

FIG. 4. Giant and gate tunable valley g factor g_ν in ABA TLG. (a) $d^3I/dV_S^3(V_S, B)$ at $V_G = 30$ V, d^3I/dV_S^3 values were numerically calculated from measured dI/dV_S values. The tunneling spectra were measured with a different calibrated STM tip and from a different location on the ABA TLG sample to where the data presented in Fig. 3 were acquired. The set point used to acquire the tunneling spectra was $I = 1$ nA, $V_S = -60$ mV, with a 2 mV ac modulation. The fanlike feature that appears at positive V_S corresponds to MLG Landau levels. (b) Simulated $\partial^2 \mathrm{LDOS}(E, B)/\partial^2 E$ at $V_G = 30$ V. The depth and width of the Gaussian potential well used in the simulation are 30 meV and 100 nm, respectively, and the γ_2 hopping was set to -10 meV. (c) Enlargement of the valley splitting peak in $d^3I/dV_S^3(V_S, B)$ at $V_G = 10$ and $V_G = 40$ V. The yellow dashed lines are the linear fits to the splitting peaks near zero B. The data are acquired with the same STM tip and set point as in (a). (d) Experimental and theoretical g_ν as a function of Δ (MLG gap size). The experimental Δ value at different V_G were extracted from the energy spacing between the LL0+ and LL0− in 0.8 T, which is schematized by the yellow arrow in (a).

To compare the observed gate tunable g_ν with a theory based on a gapped MLG QD, we use plane wave representation $\psi(\vec{k})$ of the gapped MLG QD state at $B = 0$ T to estimate the valley g factor as $g_\nu = (2/\mu_B)\int M(\vec{k})|\psi(\vec{k})|^2 d\vec{k}$ (see Supplemental Material Sec. S7 for additional details [24], which includes Refs. [40–48]). The calculated g_ν as a function of Δ for $\psi(\vec{r})$ with a Gaussian width of 150 and 300 nm are shown in Fig. 4(d)) as a green solid line and blue solid line, respectively. We determined Δ at different V_G by measuring the energy spacing between LL0− and LL0+ as shown in Fig. 4(a). The experimentally extracted g_ν as a function of Δ are plotted in Fig. 4(d), the experiment and theory display good agreement. We notice the experimental g_ν at small Δ (i.e., small V_G) agrees better with theory that corresponds to larger Gaussian width for $\psi(\vec{r})$. This is consistent with the finding in Fig. 2(b) that at lower V_G the QD has weaker confinement.

In conclusion, we fabricated high quality ABA TLG/hBN heterostructure devices and studied their gate and sublattice resolved tunneling spectra in perpendicular electric and magnetic fields. Our work shows that the effective MLG bands of ABA TLG host giant and gate tunable topological magnetic moments that can generate large and tunable valley splitting in a small B. These findings demonstrate that ABA TLG is a unique platform for fabricating valley-based quantum information devices and studying topological magnetic moment related phenomena.

We acknowledge useful discussions with Angelika Knothe, Pablo Perez Piskunow, and Joseph Weston. J. V. J. and Z. G. acknowledges support from the National Science Foundation under Grant No. DMR-1753367. J. V. J acknowledges support from the Army Research Office under Contract No. W911NF-17-1-0473. V. F. and S. S. acknowledge support from the European Graphene Flagship Core 3 Project.

V. F. acknowledges support from Lloyd Register Foundation Nanotechnology Grant, EPSRC Grants No. EP/V007033/1, No. EP/S030719/1 and No. EP/N010345/1. K. W. and T. T. acknowledge support from the Elemental Strategy Initiative conducted by the MEXT, Japan, Grant No. JPMXP0112101001, JSPS KAKENHI Grant No. JP20H00354.

*These authors contributed equally to this work.
†Vladimir.Falko@manchester.ac.uk
‡jvelasc5@ucsc.edu

[1] D. Xiao, W. Yao, and Q. Niu, Phys. Rev. Lett. **99**, 236809 (2007).
[2] S. Wu *et al.*, Nat. Phys. **9**, 149 (2013).
[3] G. Aivazian, Z. Gong, A. M. Jones, R.-L. Chu, J. Yan, D. G. Mandrus, C. Zhang, D. Cobden, W. Yao, and X. Xu, Nat. Phys. **11**, 148 (2015).
[4] K. Komatsu, Y. Morita, E. Watanabe, D. Tsuya, K. Watanabe, T. Taniguchi, and S. Moriyama, Sci. Adv. **4**, eaaq0194 (2018).
[5] H. Overweg *et al.*, Phys. Rev. Lett. **121**, 257702 (2018).
[6] R. Moriya, K. Kinoshita, J. Crosse, K. Watanabe, T. Taniguchi, S. Masubuchi, P. Moon, M. Koshino, and T. Machida, Nat. Commun. **11**, 5380 (2020).
[7] Y. Li *et al.*, Phys. Rev. Lett. **113**, 266804 (2014).
[8] D. MacNeill, C. Heikes, K. F. Mak, Z. Anderson, A. Kormányos, V. Zólyomi, J. Park, and D. C. Ralph, Phys. Rev. Lett. **114**, 037401 (2015).
[9] A. Srivastava, M. Sidler, A. V. Allain, D. S. Lembke, A. Kis, and A. Imamoğlu, Nat. Phys. **11**, 141 (2015).
[10] N. M. Freitag *et al.*, Nano Lett. **16**, 5798 (2016).
[11] M. Eich *et al.*, Phys. Rev. X **8**, 031023 (2018).
[12] N. M. Freitag *et al.*, Nat. Nanotechnol. **13**, 392 (2018).
[13] R. Kraft, I. V. Krainov, V. Gall, A. P. Dmitriev, R. Krupke, I. V. Gornyi, and R. Danneau, Phys. Rev. Lett. **121**, 257703 (2018).
[14] A. Kurzmann *et al.*, Phys. Rev. Lett. **123**, 026803 (2019).
[15] T. Wang *et al.*, Nano Lett. **20**, 694 (2020).
[16] Y. Lee *et al.*, Phys. Rev. Lett. **124**, 126802 (2020).
[17] C. Tong *et al.*, Nano Lett. **21**, 1068 (2021).
[18] X. Lu *et al.*, Nature (London) **574**, 653 (2019).
[19] A. L. Sharpe, E. J. Fox, A. W. Barnard, J. Finney, K. Watanabe, T. Taniguchi, M. Kastner, and D. Goldhaber-Gordon, Science **365**, 605 (2019).
[20] W.-Y. He, D. Goldhaber-Gordon, and K. T. Law, Nat. Commun. **11**, 1 (2020).
[21] J. Zhu, J.-J. Su, and A. H. MacDonald, Phys. Rev. Lett. **125**, 227702 (2020).
[22] H. Polshyn *et al.*, Nature (London) **588**, 66 (2020).
[23] T. Taychatanapat, K. Watanabe, T. Taniguchi, and P. Jarillo-Herrero, Nat. Phys. **7**, 621 (2011).
[24] See Supplemental Material at http://link.aps.org/supplemental/10.1103/PhysRevLett.127.136402 for (S1) sample fabrication, (S2) large scale atomically resolved topography, (S3) sublattice identification, (S4) STS data of Figs. 2(b) and 2(c) before averaging, (S5) B dependent STS data on sublattices at various V_G, (S6) band gap extraction of effective MLG bands at different V_G, (S7) theoretical model of STS on ABA TLG, (S8) localized state due to tip induced potential well, (S9) the influence of the tip potential well on the experimental detection of valley splitting in TLG, (S10) tunneling spectra on sublattice A_2, (S11) nonlinear valley splitting in ABA TLG, (S12) valley splitting of the effective BLG band in ABA TLG, (S13) linear fit to the valley splitting in B, and (S14) sublattice resolved $dI/dV_S(V_S, B)$ color plots.
[25] P. Zomer, S. Dash, N. Tombros, and B. Van Wees, Appl. Phys. Lett. **99**, 232104 (2011).
[26] A. M. Goossens, V. E. Calado, A. Barreiro, K. Watanabe, T. Taniguchi, and L. M. K. Van der sypen, Appl. Phys. Lett. **100**, 073110 (2012).
[27] Y. B. Zhang, V. W. Brar, F. Wang, C. Girit, Y. Yayon, M. Panlasigui, A. Zettl, and M. F. Crommie, Nat. Phys. **4**, 627 (2008).
[28] W. Chen, V. Madhavan, T. Jamneala, and M. F. Crommie, Phys. Rev. Lett. **80**, 1469 (1998).
[29] I. Horcas, R. Fernández, J. M. Gómez-Rodríguez, J. Colchero, J. Gómez-Herrero, and A. M. Baro, Rev. Sci. Instrum. **78**, 013705 (2007).
[30] M. Yankowitz, Q. Ma, P. Jarillo-Herrero, and B. J. LeRoy, Nat. Rev. Phys. **1**, 112 (2019).
[31] M. Koshino and E. McCann, Phys. Rev. B **79**, 125443 (2009).
[32] Y. Que, W. Xiao, H. Chen, D. Wang, S. Du, and H.-J. Gao, Appl. Phys. Lett. **107**, 263101 (2015).
[33] Y. Zhang, J.-B. Qiao, L.-J. Yin, and L. He, Phys. Rev. B **98**, 045413 (2018).
[34] J. Tersoff and D. R. Hamann, Phys. Rev. B **31**, 805 (1985).
[35] M. Yankowitz, F. Wang, C. N. Lau, and B. J. LeRoy, Phys. Rev. B **87**, 165102 (2013).
[36] M. Yankowitz, J. I-J. Wang, A. Glen Birdwell, Y.-A. Chen, K. Watanabe, T. Taniguchi, P. Jacquod, P. San-Jose, P. Jarillo-Herrero, and B. J. LeRoy, Nat. Mater. **13**, 786 (2014).
[37] Y. Zhao, J. Wyrick, F. D. Natterer, J. F. Rodriguez-Nieva, C. Lewandowski, K. Watanabe, T. Taniguchi, L. S. Levitov, N. B. Zhitenev, and J. A. Stroscio, Science **348**, 672 (2015).
[38] Y.-W. Liu, Z. Hou, S.-Y. Li, Q.-F. Sun, and L. He, Phys. Rev. Lett. **124**, 166801 (2020).
[39] A. H. Castro Neto, F. Guinea, N. M. R. Peres, K. S. Novoselov, and A. K. Geim, Rev. Mod. Phys. **81**, 109 (2009).
[40] S. Slizovskiy, A. Garcia-Ruiz, A. I. Berdyugin, N. Xin, T. Taniguchi, K. Watanabe, A. K. Geim, N. D. Drummond, and V. I. Fal'ko, Nano Lett. **21**, 6678 (2021).
[41] J. C. Slonczewski and P. R. Weiss, Phys. Rev. **109**, 272 (1958).
[42] J. W. McClure, Phys. Rev. **108**, 612 (1957).
[43] J. W. McClure, Phys. Rev. **119**, 606 (1960).
[44] M. S. Dresselhaus and G. Dresselhaus, Adv. Phys. **51**, 1 (2002).
[45] O. V. Gamayun, E. V. Gorbar, and V. P. Gusynin, Phys. Rev. B **83**, 235104 (2011).
[46] S. Slizovskiy, Phys. Rev. B **92**, 195426 (2015).
[47] C. W. Groth, M. Wimmer, A. R. Akhmerov, and X. Waintal, New J. Phys. **16**, 063065 (2014).
[48] A. Weiße, G. Wellein, A. Alvermann, and H. Fehske, Rev. Mod. Phys. **78**, 275 (2006).